CN 21-1611/TQ
ISSN 2667-2669

CORROSION COMMUNICATIONS

腐蚀学报（英文） March 2025 Volume 17

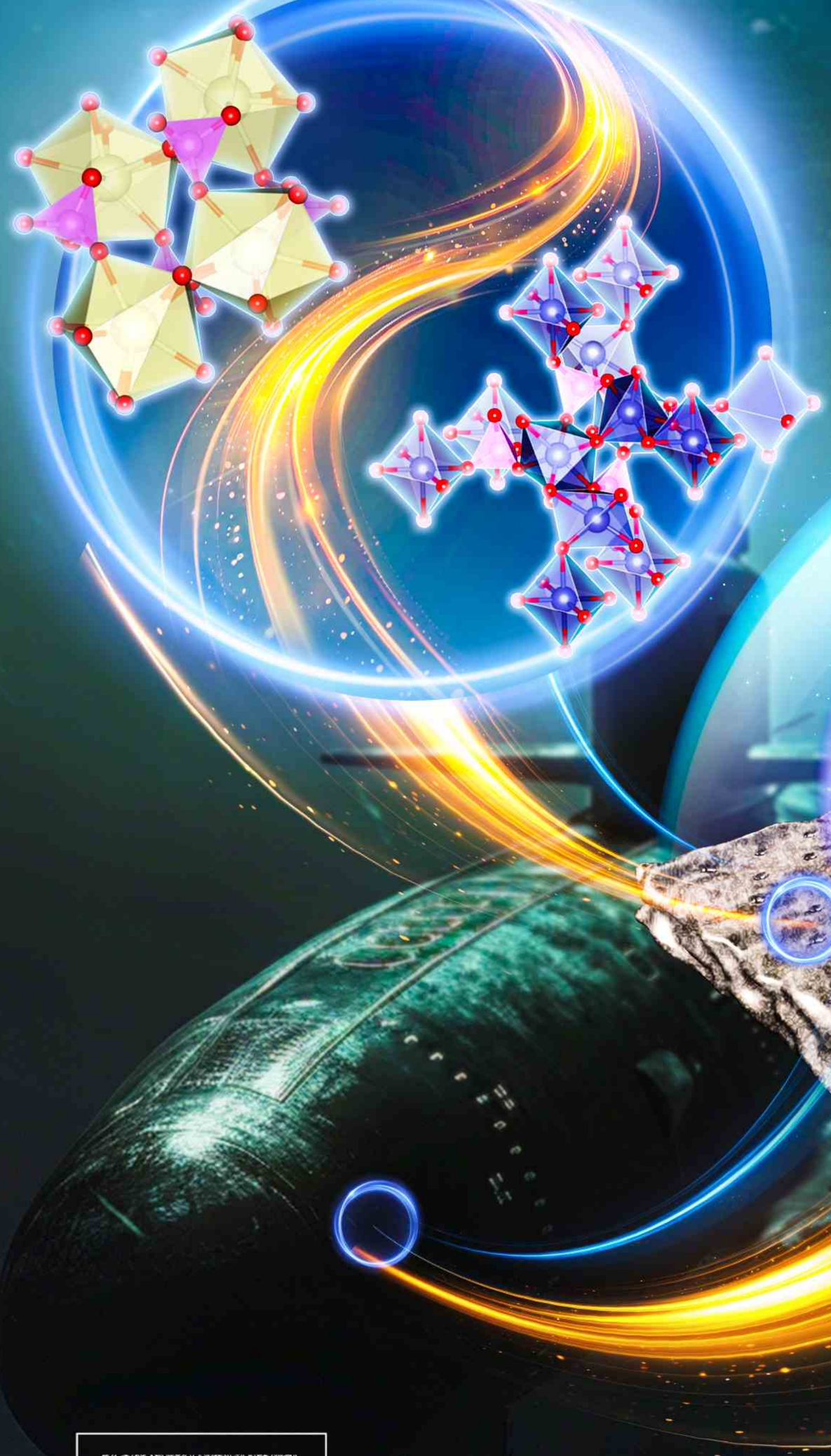

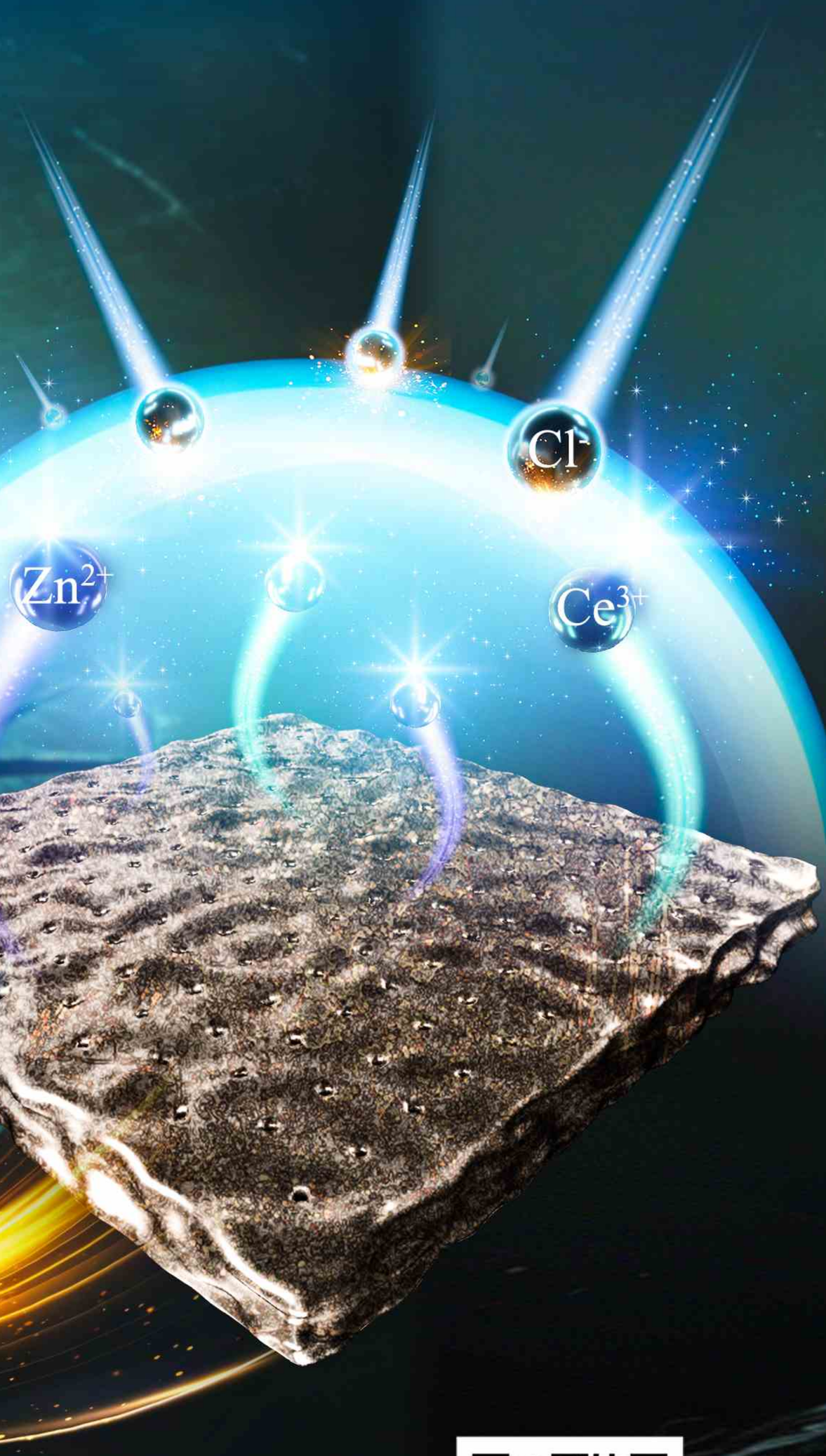

Sponsored by
Institute of Metal Research, Chinese Academy of Sciences

Corrosion Communications 17 (2025) 35–43

Contents lists available at ScienceDirect

Corrosion Communications

journal homepage: www.elsevier.com/locate/corcom

Research Article

Enhancing corrosion resistance of MAO coatings on Al alloy LY12 through *in situ* co-doping with zinc phosphate and cerium phosphate

Chao Yang[a], Tao Ying[a], Aihui Huang[b,*], Jian Huang[d], Pinghu Chen[c,*], Paul K. Chu[e], Xiaoqin Zeng[a]

[a] National Engineering Research Center of Light Alloy Net Forming, School of Materials Science and Engineering, Shanghai Jiao Tong University, Shanghai 200240, China
[b] Shanghai Key Laboratory of Advanced High-Temperature Materials and Precision Forming, School of Materials Science and Engineering, Shanghai Jiao Tong University, Shanghai 200240, China
[c] College of Mechanical Engineering, Key Laboratory of Hunan Province of Equipment Safety Service Technology under Extreme Environment, University of South China, Hengyang 421001, China
[d] Department of Chemistry, University of Munich (LMU), Munich 81377, Germany
[e] Department of Physics, Department of Materials Science & Engineering, and Department of Biomedical Engineering, City University of Hong Kong, Hong Kong 999077, China

ARTICLE INFO

Article history:
Received 26 August 2024
Received in revised form 10 October 2024
Accepted 10 October 2024
Available online 31 January 2025

Keywords:
Aluminum alloys
Micro-arc oxidation coating
Corrosion resistance
Zinc phosphate
Cerium phosphate

ABSTRACT

Corrosion of aluminum (Al) alloys during service limits many applications. Micro-arc oxidation (MAO) coatings can enhance corrosion resistance, but porous defects in the films undermine their effectiveness. Here, by mixing a phosphate electrolyte with soluble Zn and Ce salts, zinc phosphate and cerium phosphate co-doped MAO corrosion-resistant coating is prepared on Al alloy LY12. Zinc phosphate and cerium phosphate are incorporated *in situ* to form an amorphous encapsulated nanocrystalline structure. During long-term corrosion, Zn^{2+} is released and deposited as corrosion products $Zn(OH)_2$ to cover weak corrosion micro-regions in the coating. Simultaneously, Ce^{3+} released from MAO coating co-doped with zinc phosphate/cerium phosphate forms $Zn(OH)_2/Ce(OH)_3$ due to the small solubility product K_{sp} to further enhance corrosion resistance. Compared to pristine Al alloy, corrosion potential increases from -1.306 to -0.819 V_{SCE}, and corrosion current density decreases by 4 orders of magnitude from 2.6×10^{-6} to 2.5×10^{-10} A·cm^{-2}. Co-doped MAO coating significantly enhances corrosion resistance of Al alloy LY12 and shows great potential for a wide range of applications.

1. Introduction

Aluminum (Al) and its alloys offer advantages such as low density, high strength, and easy processing, making them suitable for a wide range of applications in aviation, aerospace, marine, automotive, and 3C electronics industries [1,2]. However, Al alloys are prone to corrosion in high salt and humidity environments as well as cycling between high and low temperatures [3–5]. Surface coatings produced by chemical conversion, anodizing, micro-arc oxidation (MAO), cold/hot spraying, physical vapor deposition, and chemical vapor deposition can provide surface protection to Al alloys [6–8]. For example, MAO produces an oxide layer composed of inert Al oxide [9,10]. However, owing to the discharge environments, these coatings normally have pores that allow external corrosive medium to penetrate and create local corrosion [11,12]. Therefore, optimizing the porous structure is crucial to improve corrosion resistance of MAO coatings upon Al alloys.

Pore sealing reduces permeation of corrosive medium and enhances corrosion resistance of MAO coatings. The process typically involves organic secondary sealing and nanoparticle sealing [13,14]. Organic secondary sealing is prone to aging and failure during prolonged use, especially under harsh conditions [15]. Nanoparticle sealing is challenging to achieve stable and uniform incorporation of nanoparticles in harsh MAO environment, resulting in unclear sealing effects [16–18]. Alternatively, tailoring electrolyte can achieve same objective and surface strengthening can be accomplished at weak points in MAO coatings [19]. Ji et al. have prepared MAO coatings doped with iron phosphate and aluminum phosphate on Al alloy LY12 surfaces by designing electrolytes containing P and Fe [20]. Neutral salt spray lifetime is as high

* Corresponding authors.
E-mail addresses: huangaihuivip@sjtu.edu.cn (A. Huang), chenping-hu1986@163.com, chaoyang0315@163.com (P. Chen).

https://doi.org/10.1016/j.corcom.2024.10.001

as 1800 h, and passivation potential is higher than 10 V, exhibiting excellent corrosion resistance. Yang et al. have doped Ce salt onto Al alloy, constructing a hydrophobic surface [21]. This process significantly improves material's corrosion resistance while also exhibiting antibacterial properties.

Huang et al. have demonstrated that MAO coatings prepared on Al alloy using phosphate and zinc acetate electrolytes exhibit enhanced corrosion resistance [22]. This improvement can be attributed to the release of Zn^{2+} during corrosion and subsequent formation of $Zn(OH)_2$ corrosion product as pore fillers. Typically, the faster the corrosion product precipitates, the better the pore blocking effect on pitting corrosion [23–25]. Therefore, easily precipitated metals may be able to produce pronounced effects. The K_{sp} of Ce^{3+} for the formation of the $Ce(OH)_3$ precipitate is less than that of $Zn(OH)_2$ (K_{sp} ($Ce(OH)_3$) = 1×10^{-20}, K_{sp} ($Zn(OH)_2$) = 1.2×10^{-12}), and cerium salts can exist stably in phosphate electrolytes [26]. Therefore, a dual-phase system containing Ce may produce better corrosion resistance. However, there is a lack of research on the specific effects of doping with this dual functional phase on structure and corrosion behavior of MAO coatings.

In this study, phosphate electrolyte is chosen as main salt, with soluble Zn and Ce salts being precursors. Zinc phosphate/cerium phosphate co-doped corrosion-resistant MAO coating is prepared on Al alloy LY12. Composition and structure are systematically determined using XRD, XPS and TEM. Corrosion resistance is examined through electrochemical tests, and corrosion resistance mechanism is explored by immersion tests in NaCl electrolyte.

2. Experimental

2.1. Materials

Al alloy LY12 (50 mm × 25 mm × 1 mm) was purchased from Shanghai Bixuan Metal Materials Co., Ltd. Analytical-grade chemical reagents, including anhydrous ethanol, sodium hydroxide, sodium chloride, and sodium hexametaphosphate, were purchased from China National Pharmaceutical Group Chemical Reagent Co., Ltd. (Shanghai, China). Zinc acetate, cerium acetate, and disodium ethylenediaminetetraacetate were bought from Aladdin Bio-Chem Technology Co., Ltd. (Shanghai, China). All reagents were used without purification.

2.2. Coating preparation

Al alloy LY12 was polished with 2000 grit sandpaper and cleaned sequentially with deionized water and anhydrous ethanol ultrasonically for 10 min. MAO electrolyte contained 20 g/L sodium hexametaphosphate, 3 g/L sodium hydroxide, and 5 g/L EDTA-2Na. Zn15 coatings were prepared by adding 15 g/L zinc acetate to electrolyte, and those produced by separately adding 5 and 10 g/L cerium acetate were designated as Zn15Ce5 and Zn15Ce10. MAO was conducted using a 15 kW AC power supply in constant current mode, with Al sample as anode and an equal-size stainless steel plate as cathode, at a current density of 5 $A{\cdot}dm^{-2}$, frequency of 500 Hz, duty cycle of 15 %, and discharge time of 10 min. During MAO, water was circulated to maintain temperature below 45 °C.

2.3. Electrochemical and corrosion assessments

Electrochemical and immersion tests were conducted on Al alloy and MAO coatings. An electrochemical workstation (Gamry 1010E) with a three-electrode cell system was utilized at room temperature, with 3.5 % (mass fraction) NaCl solution serving as electrolyte. The sample functioned as working electrode, while the saturated calomel electrode (SCE) and Pt served as reference and counter electrodes, respectively. 30-minute open circuit potential (OCP) operation was carried out to stabilize the system. Electrochemical impedance spectroscopy (EIS) was performed within a frequency range of 10^5–10^{-1} Hz using a sinusoidal signal of 10 mV. The data obtained were analyzed using the ZsimpWin software. Tafel data was collected at a scanning rate of 1 mV/s, with corrosion potential and corrosion current density calculated through Tafel extrapolation. For immersion experiment, samples were immersed in 3.5 wt. % NaCl solution for 14 d in triplicate.

2.4. Characterization

Scanning electron microscopy (SEM, Carl Zeiss, SUPRA® 55), energy-dispersive X-ray spectroscopy (EDS), transmission electron microscopy (TEM, JEM-3200FS), X-ray diffraction (XRD, Bruker, D8 Advance), and X-ray photoelectron spectroscopy (XPS, Thermo Fisher, ESCALAB 250X) were used to analyze samples. Cross-sections were prepared by focused ion beam (FIB, Scios, FEI), and 3D laser confocal scanning microscopy (LCSM, VK-X200 series) was carried out to examine surface contours and roughness.

3. Results and discussion

Fig. 1 displays surface morphology of various MAO coatings on Al alloy LY12. Undoped MAO coating exhibits densely distributed pores ranging from 1 to 3 μm, resembling the molten form created by liquid plasma discharge. In Zn15 coating, pores are slightly larger (5 – 8 μm) with nanoparticles observed inside pores and on walls, playing a crucial role in sealing pores in situ. In comparison, Zn15, Zn15Ce5 and Zn15Ce10, which are co-doped with zinc phosphate and cerium salt, have a larger pore size of around 10 μm but in smaller quantities. It is due to the dual-metal salt electrolyte increasing the discharge and plasma arc size at higher voltages, resulting in larger pores.

However, breakdown difficulty of multi-phase doped MAO coatings increases, decreasing the number of pores. Nanoparticles are also present on pores and walls of Zn15Ce5 and Zn15Ce10, albeit significantly larger, appearing as zinc and cerium precipitates formed at high voltages. LCSM analysis indicates that zinc phosphate doping increases the surface roughness of the MAO coatings. Furthermore, co-doping with cerium salt further enhances surface roughness R_a, correlating with the trend of changes in pore size resulting from intensified discharge due to dual-metal salt doping (Fig. 1(d)).

Fig. 2 depicts cross-sectional morphology and elemental distribution of MAO coatings on Al alloy LY12. Thicknesses of MAO, Zn15, Zn15Ce5, and Zn15Ce10 are 25.2 ± 2.1, 25.4 ± 2.2, 24.6 ± 3.7, and 25.1 ± 1.5 μm, respectively, indicating that Zn salt and Ce salt have no effect on thickness of the coatings. Cross-sectional morphology of MAO coating is consistent with surface morphology revealing a porous structure. It is caused by liquid plasma discharge, leading to splattering and reacting with electrolyte to form mixed oxide coating. There are still a small number of pores that are not completely filled, as evidenced by irregular porous structure inside. EDS results show the presence of Al, O, and P. Zn15 doped with zinc phosphate reveals the presence of Zn across the entire cross-section, with accumulation at the pores due to the local liquid plasma discharge promoting the generation of zinc phosphate. In comparison, Zn15Ce5 and Zn15Ce10 show Zn and Ce throughout cross-section, with Ce, Al, P and O being uniformly distributed, and Zn enriched in pore positions. It may be related to the small K_{sp} of zinc phosphate (9.1×10^{-33}) and the tendency to preferentially form at pores [27], while substances such as cerium phosphate and aluminum oxide are uniformly generated in the coating.

Fig. 3(a) displays elemental composition and concentration of various coatings. Similar to EDS results of cross-section, MAO coating consists of Al, O, and P. The coatings doped with Zn and Ce salts have Zn and Ce, respectively. P concentration in MAO coating is only 2.9 % (atomic fraction), indicating that primary phase of the coating is aluminum oxide. In comparison, P concentrations in Zn15, Zn15Ce5, and Zn15Ce10 are 10.8 %, 12.1 %, and 15.0 %, respectively. The significant increase in P content in MAO coatings doped with zinc acetate or cerium acetate can

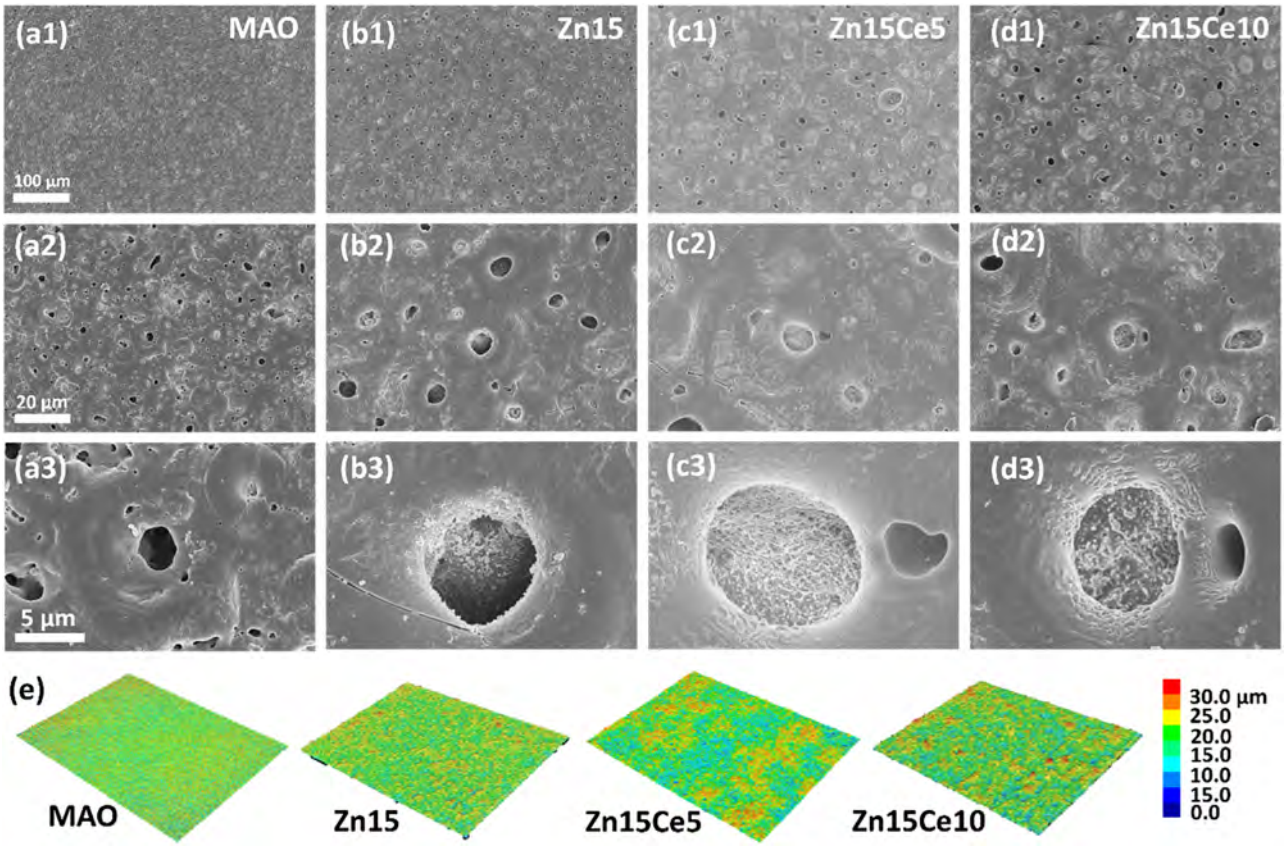

Fig. 1. SEM images of undoped and doped MAO coatings: (a) MAO, (b) Zn15, (c) Zn15Ce5, (d) Zn15Ce10, (e) LCSM images of all samples.

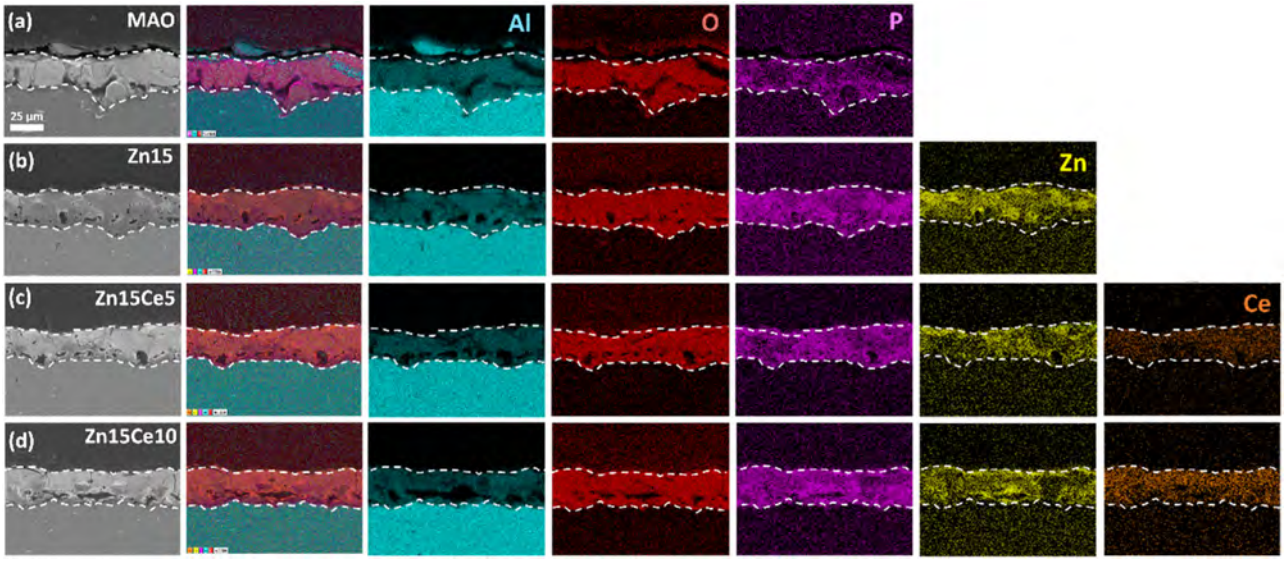

Fig. 2. Cross-sectional SEM images and EDS maps of undoped and doped MAO coatings on Al alloy LY12: (a) MAO, (b) Zn15, (c) Zn15Ce5, and (d) Zn15Ce10.

be attributed to the generation of zinc phosphate and cerium phosphate with lower K_{sp} under higher voltage.

In contrast, for ordinary MAO coatings, Al is more likely to form aluminum oxide rather than aluminum phosphate, as confirmed by the subsequent coating phase structure results. Similarly, Zn concentrations in Zn15, Zn15Ce5, and Zn15Ce10 are 9.03 %, 10.12 %, and 10.29 %, respectively. The slight enhancement in zinc phosphate content indicates that there is no competitive doping of Zn salt and Ce salt during MAO due to the copious supply of phosphate ions from the electrolyte. Ce concentrations in Zn15Ce5 and Zn15Ce10 are 2.6 % and 4.6 %, respectively, consistent with solubilities. In fact, zinc phosphate with a lower solubility typically forms before cerium phosphate, thus ensuring complete incorporation of Zn in the process.

Fig. 3(b-d) presents chemical composition and phase composition of various coatings. XRD results reveal Al, α-Al_2O_3, and γ-Al_2O_3 (Fig. 3(b)). Compared to undoped MAO coating, Zn15, Zn15Ce5, and Zn15Ce10 show peaks between 20° and 35°, indicating the formation of amorphous phases due to harsh MAO discharge and rapid coating formation

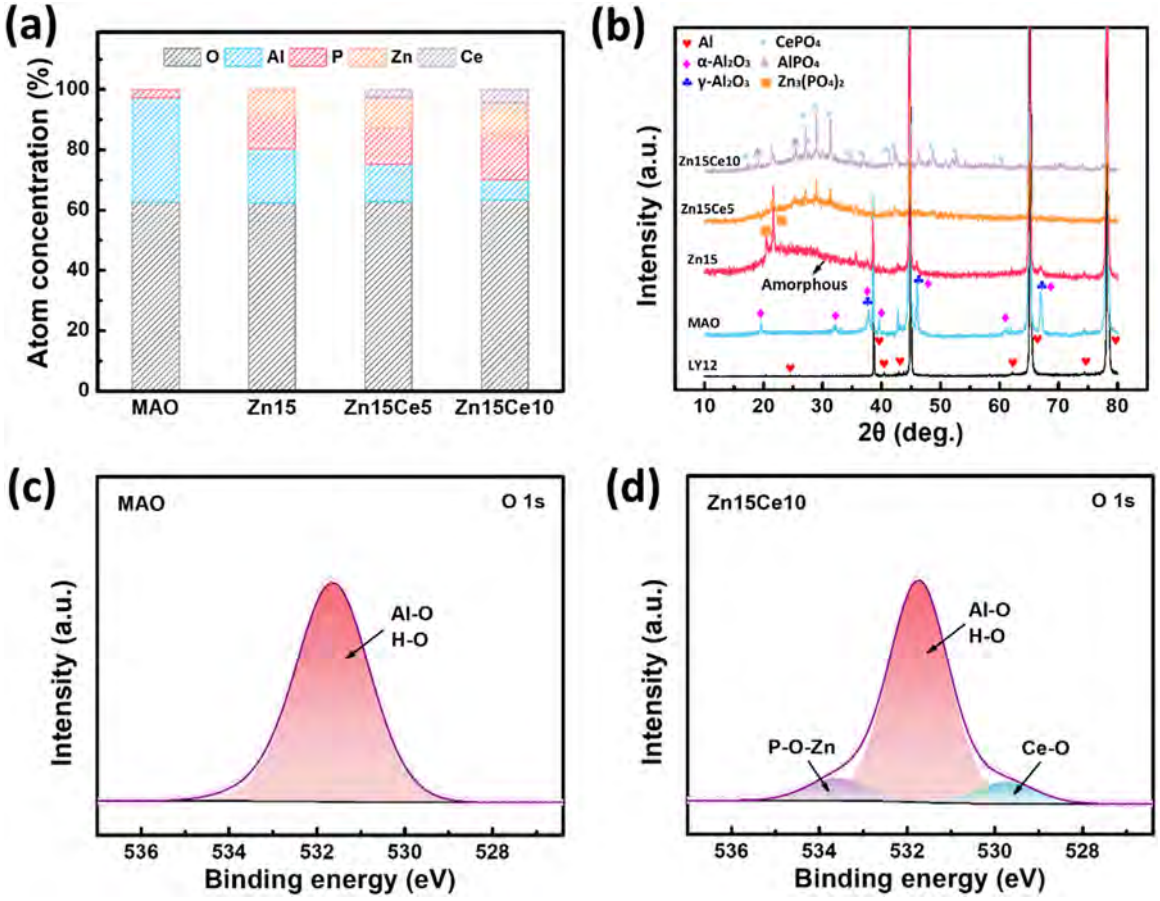

Fig. 3. (a) Phases and chemical composition of undoped/doped MAO coatings on Al alloy LY12, (b) XRD spectra; XPS O 1 s spectra of (c) undoped MAO and (d) Zn15Ce10 coating.

[28]. Furthermore, Zn15 exhibits characteristic peaks of $Zn_3(PO_4)_2$ at 20.8° and 21.9°, indicating the formation of highly corrosion-resistant zinc phosphate. Zn15Ce5 and Zn15Ce10 not only show zinc phosphate but also multiple peaks from cerium phosphate in the range of 15°–60°, along with peaks from aluminum phosphate. XPS shows consistent results, with Al-O and H–O bonds at 531.5 eV observed from both MAO and Zn15Ce10, indicative of alumina (Fig. 3(c, d)) [29]. Zn15Ce10 shows peaks from Ce-O and P-O-Zn bonds at 529.6 and 533.5 eV, respectively, confirming the formation of cerium phosphate and zinc phosphate in the coating [30,31].

FIB is performed to prepare Zn15Ce10 cross-section for TEM (Fig. 4). EDS results of the small-size cross-section are consistent with the results from the larger sample, indicating uniform doping for each element (Fig. 4(a)). TEM images show that surface of the coating, which is approximately 150 nm deep, is amorphous (Fig. 4(b-e)) due to rapid cooling in the liquid electrolyte. Generally, amorphous phases exhibit greater resistance to corrosion compared to crystalline phases because of the absence of microstructural defects such as grain boundaries. Fig. 4(f) displays microstructure beneath the amorphous layer, revealing a combination of amorphous and nanocrystalline phases. High-resolution TEM analysis reveals that the nanocrystals primarily consist of α-Al_2O_3 (210), $Zn_3(PO_4)_2$ (021), and $CePO_4$ (101) (Fig. 4(g, h)). There is no distinct interface between nanocrystals and amorphous regions due to the energetic discharge during MAO process. Selected-area electron diffraction (SAED) patterns support the presence of mixed amorphous/crystalline regions (Fig. 4(i)).

Tafel assessment was conducted on Al alloy LY12 and MAO coatings in 3.5 wt. % NaCl solution to determine corrosion trend, and results are presented in Fig. 5 and Table 1. Corrosion potential increased from −1.306 V_{SCE} of bare substrate to −1.253 V_{SCE} of MAO, and the corrosion current density decreased gradually from 2.6×10^{-6} A·cm^{-2} of substrate to 9.8×10^{-9} A·cm^{-2} of MAO. After doping with zinc phosphate, corrosion potential of Zn15 increased significantly to −0.817 V_{SCE}, while corrosion current density decreased to 6.2×10^{-10} A·cm^{-2}. However,

Table 1
Corrosion potentials and corrosion current densities of Al alloy LY12 and undoped/doped MAO coatings.

Sample	Corrosion potential / V_{SCE}	Corrosion current density / A·cm^{-2}	Breakdown potential / V_{SCE}	R_p / Ω·cm^2
LY12	−1.306	2.6×10^{-6}	—	7.9×10^2
MAO	−1.253	9.8×10^{-9}	−1.056	6.2×10^3
Zn15	−0.817	6.2×10^{-10}	−0.574	3.9×10^4
Zn15Ce5	−0.824	3.7×10^{-10}	−0.487	4.5×10^4
Zn15Ce10	−0.819	2.5×10^{-10}	−0.392	4.9×10^4

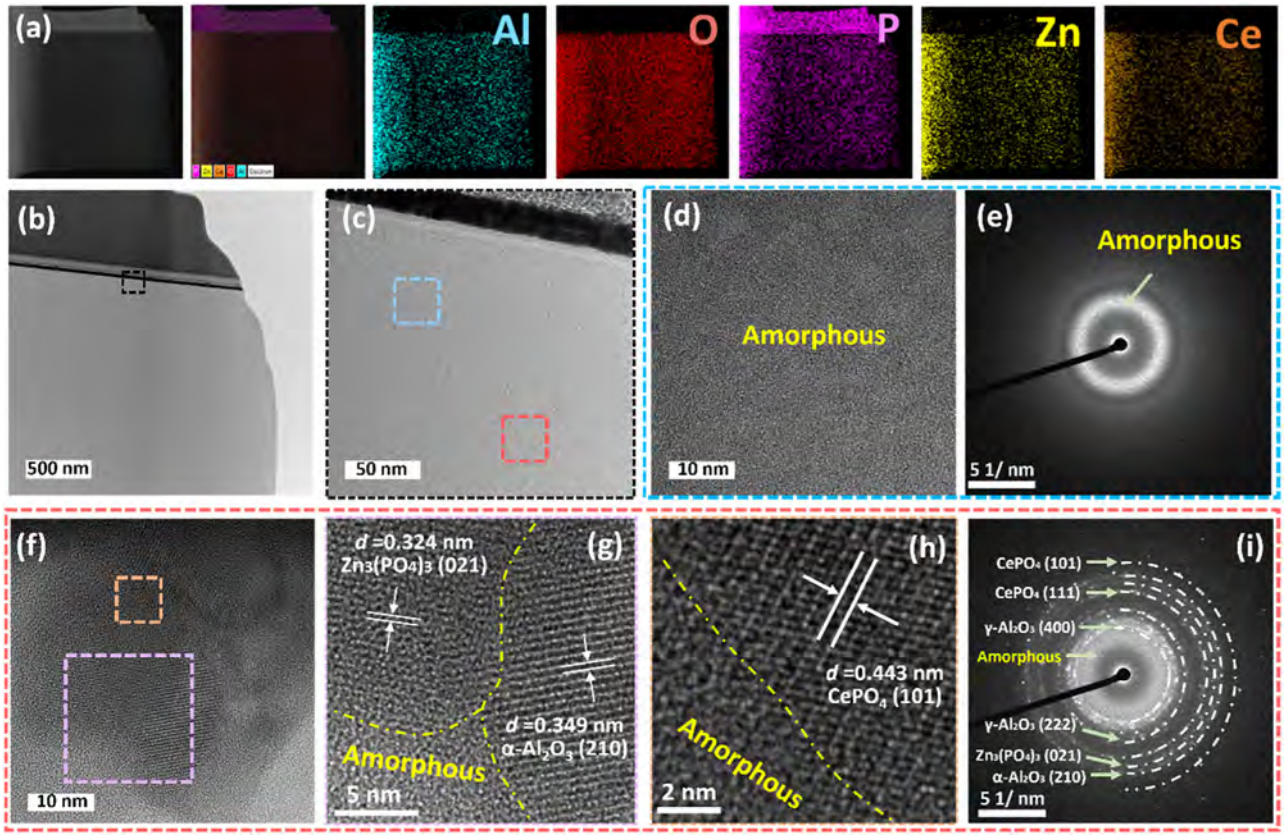

Fig. 4. TEM images of the cross-section of Zn15Ce10: (a) EDS maps, (b, c) low-resolution TEM images, (c) TEM image of the black box in Fig. 4(b), (d) high-resolution TEM image, (e) SAED pattern of the blue box in Fig. 4(c), (f) high-resolution TEM image of the red box in Fig. 4(c); (g, h) high-resolution images and (i) SAED pattern of the area in Fig. 4(f).

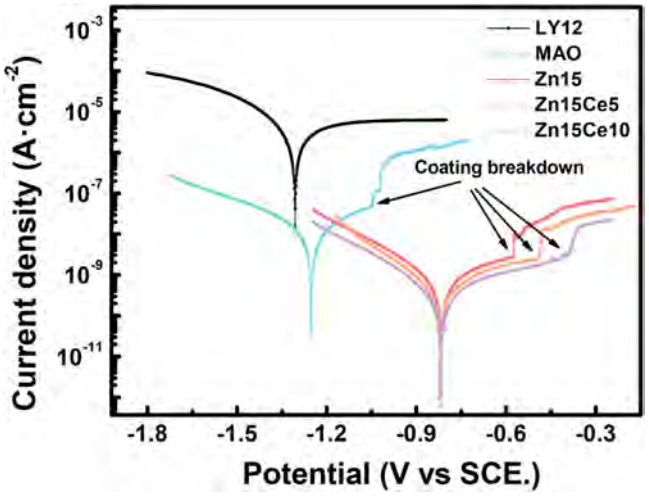

Fig. 5. Tafel curves of Al alloy LY12 and undoped/doped MAO coatings.

after further co-doping with cerium phosphate, corrosion potentials of Zn15Ce5 and Zn15Ce10 coatings remained at −0.8024 and −0.819 V_{SCE}, respectively. Nevertheless, corrosion current densities of Zn15Ce5 and Zn15Ce10 diminished to 3.7×10^{-10} and 2.5×10^{-10} A·cm^{-2}, respectively. In addition, breakdown potential of MAO coating in anodic curve increased after doping with zinc phosphate and cerium phosphate, with the potentials of MAO, Zn15, Zn15Ce5, and Zn15Ce10 being −1.056, −0.574, −0.487, and −0.392 V_{SCE}, respectively.

In addition, polarization resistance (R_p) is inversely proportional to corrosion rate and it can be calculated by the Stern-Gear formula as shown in formula (1) [32,33]:

$$R_p = \frac{\beta_a \beta_c}{2.3 i_{corr}(\beta_a + \beta_c)} \quad (1)$$

where, β_a and β_c are the absolute values of two slopes near the extreme point in the Tafel curves. Table 1 indicates that the R_p increases to 4.9×10^4 Ω·cm^2 (Zn15Ce10), which is two times larger than that of Al alloy LY12 (7.9×10^2 Ω·cm^2). Therefore, the significant increase in R_p of the coating with the coexistence of zinc phosphate and cerium phosphate promotes a significant decrease in the electrochemical activity of the coating. The incorporation of zinc phosphate and cerium phosphate improves the corrosion resistance. These results indicate that the MAO coatings enhance passivation protection, while zinc phosphate improves corrosion resistance. Co-doping with zinc phosphate and cerium phosphate further enhances the corrosion resistance by inhibiting the penetration of salt solution to Al alloy LY12.

EIS is performed to analyze the corrosion resistance of Al alloy LY12 and MAO coatings in 3.5 % NaCl solution. Nyquist results reveal the distinctive capacitive behavior during immersion (Fig. 6(a)). Compared to the substrate, the capacitive loop diameter of the MAO coatings and after zinc phosphate doping and zinc phosphate/cerium phosphate co-doping increases gradually. Generally, the low-frequency impedance modulus in the Bode impedance plot, which represents the overall impedance, increases by >3 orders of magnitude compared to bare substrate from 1.3×10^2 to 3.0×10^5 Ω·cm^2, while Zn15, Zn15Ce5, and Zn15Ce10 exhibit higher low-frequency resistances in the salt solution of 5.0×10^6, 1.2×10^7, and 1.8×10^7 Ω·cm^2, respectively. Hence, co-doping with zinc phosphate and cerium phosphate enhances corrosion resistance of MAO coatings (Fig. 6(b)).

According to the time constant in Bode phase angle diagram in Fig. 6(c), the equivalent circuit used to fit and analyze the EIS data

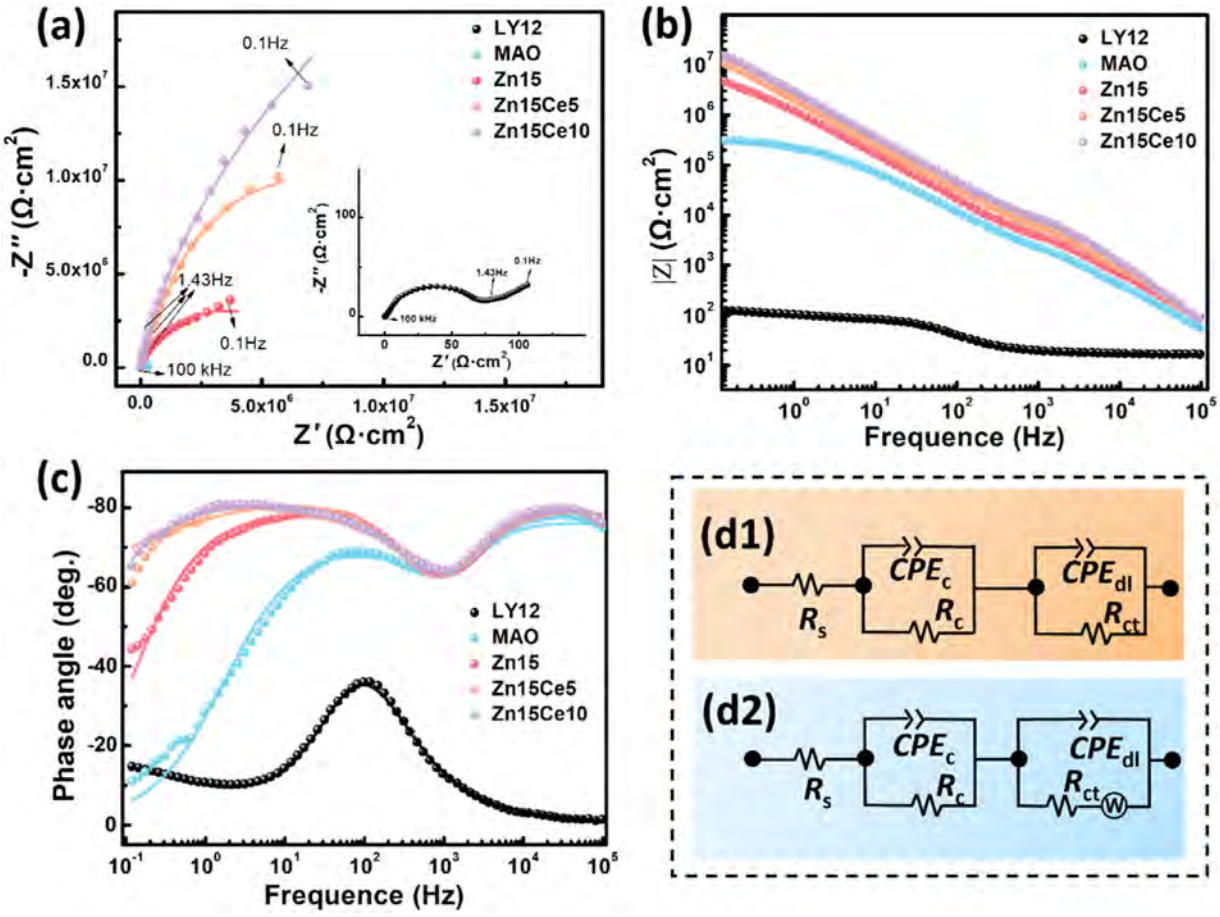

Fig. 6. EIS data and fitted results of Al alloy LY12 and undoped/doped MAO coatings: (a) Nyquist plots, (b) Bode-impedance plots, (c) Bode-phase angle plots, and equivalent circuits of (d1) LY12 alloy and (d2) MAO coatings.

is derived (Fig. 6(d)). The capacitance loop observed at medium and high frequencies is associated with MAO coating, whereas the electrochemical activity at low frequencies is linked to the interfacial reaction between coating and substrate within salt solution. Typically, coating's surface exhibits a rough and porous structure, with potentially uneven distribution of chemical components, leading to non-uniformity during testing. Consequently, traditional capacitors and resistors are not suitable for analyzing the charge transfer process at interface. In this case, a constant phase element (CPE) is adopted to describe the unevenness of the coating, as shown in formula (2) [34]:

$$Z_{\mathrm{CPE}} = \frac{1}{T(j\omega)^n} \qquad -1 \le n \le 1 \tag{2}$$

where Z_{CPE} represents the resistance of CPE, T is the CPE coefficient, $j = \sqrt{-1}$ is the imaginary number, ω is the angular frequency (related to the frequency f by $\omega = 2\pi f$), and n is the CPE index. When n is −1, 0, and 1, it is, respectively, simulated as an ideal inductor, resistor, and capacitor. The EIS data of substrate and MAO coating are fitted by the capacitor circuit in Fig. 6(d1), and the high capacitance arc radii of Zn15, Zn15Ce5, and Zn15Ce10 are fitted with the added Warburg resistance (Fig. 6(d2)). Here, $\mathrm{CPE_c}$ and R_c are the constant phase element capacitor and resistance of the passivation layer or MAO coating on the substrate, $\mathrm{CPE_{dl}}$ and R_{ct} represent the double layer capacitance and charge transfer resistance in the Faraday process, and W is the Warburg resistance in the ion diffusion process.

Table 2 presents the changes in the constant phase element capacitances and resistances of the LY12 alloy and MAO coatings in the salt solution. After MAO, $\mathrm{CPE_c}$ decreases from 5.2×10^{-3} to 6.2×10^{-6} $\Omega^{-1}\cdot\mathrm{cm}^{-2}\cdot s^n$. $\mathrm{CPE_c}$ values of Zn15, Zn15Ce5, and Zn15Ce10 decrease to 1.1×10^{-8}, 5.4×10^{-9}, and 2.8×10^{-9} $\Omega^{-1}\cdot\mathrm{cm}^{-2}\cdot s^n$. The change in $\mathrm{CPE_{dl}}$ is consistent with $\mathrm{CPE_c}$, with the LY12 substrate, MAO, Zn15, Zn15Ce5, and Zn15Ce10 dropping to 7.5×10^{-3}, 3.4×10^{-6}, 5.6×10^{-8}, 6.7×10^{-9}, and 1.9×10^{-9} $\Omega^{-1}\cdot\mathrm{cm}^{-2}\cdot s^n$, respectively. In contrast, the resistance change is opposite to that of the capacitance, manifested by the substrate resistance R_c increasing from 1.7×10^2 to 1.0×10^3 $\Omega\cdot\mathrm{cm}^2$ after MAO. After zinc phosphate doping and zinc phosphate/zinc cerium co-doping, R_c increases to 6.8×10^4, 9.5×10^4, and 2.7×10^5 $\Omega\cdot\mathrm{cm}^2$ for Zn15, Zn15Ce5, and Zn15Ce10, respectively. Correspondingly, R_{ct} also exhibits an increasing trend, with R_{ct} of Zn15Ce10 increasing by over 5 orders of magnitude compared to Al alloy LY12 substrate. Hence, Zn15Ce10 has the highest corrosion resistance.

Fig. 7 shows corrosion morphology of MAO coating samples after immersion in 3.5 wt.% NaCl for 14 d. Dense cracks and pores are observed from MAO coating, and upon magnification, a large amount of loose corrosion products can be clearly observed. Based on EDS and previous studies, corrosion product is $Al(OH)_3$ [35]. In the salt solution, Cl^- erode $Al(OH)_3$ to form cracks or pores, giving rise to insufficient corrosion resistance (Fig. 7(a)). In comparison, Zn15 doped with zinc phosphate shows almost no cracks after 14 d, but there are many layer-like corrosion products (Fig. 7(b)). These structures are mainly found inside and around the edges of the pores, where the corrosion medium and ions tend to accumulate to produce more severe corrosion.

MAO coating doped with zinc phosphate releases Zn^{2+} during immersion to react with OH^- to generate corrosion product of $Zn(OH)_2$, which is deposited near pores (Fig. 7(b4)). It effectively seals off the corrosion micro-regions in pores. With regard to Zn15Ce5 co-doped with zinc phosphate and cerium phosphate, only a small amount of local corrosion products is observed after 14 d (Fig. 7(c4)). The mixed corrosion

Table 2
EIS fitted data of Al alloy LY12 and undoped/doped MAO coatings.

Sample	R_s ($\Omega \cdot cm^2$)	CPE_c ($\Omega^{-1} \cdot cm^{-2} \cdot s^n$)	n_c	R_c ($\Omega \cdot cm^2$)	W ($S \cdot sec^{0.5} \cdot cm^{-2}$)	CPE_{dl} ($\Omega^{-1} \cdot cm^{-2} \cdot s^n$)	n_{dl}	R_{ct} ($\Omega \cdot cm^2$)	χ^2
LY12	27.8	5.2×10^{-3}	0.82	1.7×10^2	—	7.5×10^{-3}	0.89	1.3×10^3	2.1×10^{-3}
MAO	28.2	6.2×10^{-6}	0.91	1.0×10^3	—	3.4×10^{-6}	0.73	3.4×10^5	4.8×10^{-3}
Zn15	28.4	1.2×10^{-8}	0.87	6.8×10^4	4.9×10^{-8}	5.6×10^{-8}	0.77	7.8×10^7	4.2×10^{-3}
Zn15Ce5	30.5	5.4×10^{-9}	0.95	9.5×10^4	1.9×10^{-8}	6.7×10^{-9}	0.84	3.3×10^8	3.8×10^{-3}
Zn15Ce10	28.3	2.8×10^{-9}	0.88	2.7×10^5	7.3×10^{-9}	1.9×10^{-9}	0.92	7.3×10^8	4.3×10^{-3}

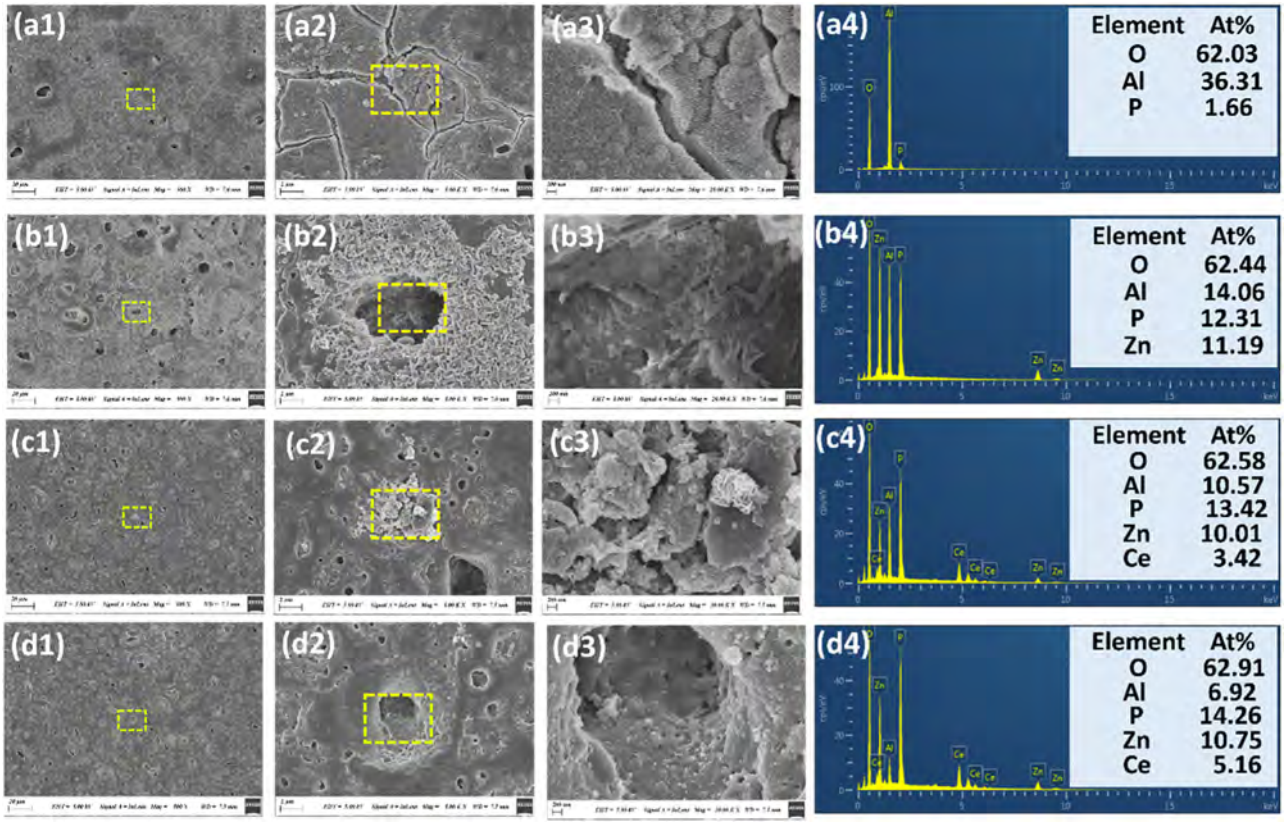

Fig. 7. SEM and EDS images of undoped and doped MAO coatings on Al alloy LY12 after immersion in salt solution for 14 d: (a) MAO, (b) Zn15, (c) Zn15Ce5, (d) Zn15Ce10.

products of $Zn(OH)_2$ and $Ce(OH)_3$ [31] seal off the vulnerable corrosion micro-regions. Surface of Zn15Ce10 doped with more cerium shows almost no pitting corrosion after 14 d (Fig. 7(d)).

In this study, MAO coatings doped with zinc phosphate/cerium phosphate are prepared on Al alloy LY12 to seal the inherent pores and improve corrosion resistance. The corrosion mechanism is analyzed and illustrated in Fig. 8. In undoped MAO coating on Al alloy LY12 surface, main component is corrosion-resistant Al_2O_3. Although it is difficult to corrode in Cl^- environment, there are many weak pores on surface and in MAO coating. During long-term immersion, Cl^- can penetrate the coating *via* defects to corrode the substrate, leading to the dissolution and corrosion of Al, as shown by formula (3):

$$Al \rightarrow Al^{3+} + 3e^- \quad (3)$$

The electrons generated undergo oxygen absorption or hydrogen evolution at the interface [36,37] as shown by formulas (4) and (5):

$$O_2 + 2H_2O + 4e^- \rightarrow 4OH^- \quad (4)$$

$$2H_2O + 2e^- \rightarrow H_2 + 2OH^- \quad (5)$$

Al^{3+} and OH^- generated at the corrosion interface react to produce the corrosion product of $Al(OH)_3$, which is then deposited on the corroded surface, as shown by formula (6):

$$Al^{3+} + 3OH^- \rightarrow Al(OH)_3 \quad (6)$$

However, $Al(OH)_3$ is attacked by Cl^- to form the loose corrosion product of $Al(OH)_{3-n}Cl_n$ (n = 1, 2, 3) [38], as shown by formula (7):

$$Al(OH)_3 + nCl^- \rightarrow Al(OH)_{3-n}Cl_n + nOH^- \ (n = 1, 2, 3) \quad (7)$$

The loose corrosion products are susceptible to hydrolysis and pitting corrosion. During immersion, pitting corrosion occurs cyclically at these weak areas, ultimately resulting in severe corrosion and coating failure.

In the MAO coatings doped with zinc phosphate, zinc phosphate is evenly distributed in the main phase of the aluminum oxide coating and tends to accumulate at weak points due to local discharge. In-situ generated zinc phosphate, Al_2O_3, and cerium phosphate exist in amorphous form on the outermost layer of the coating. The combination of the amorphous structure and lower K_{sp} substances promotes the coating to exhibit higher corrosion resistance, resulting in a higher corrosion po-

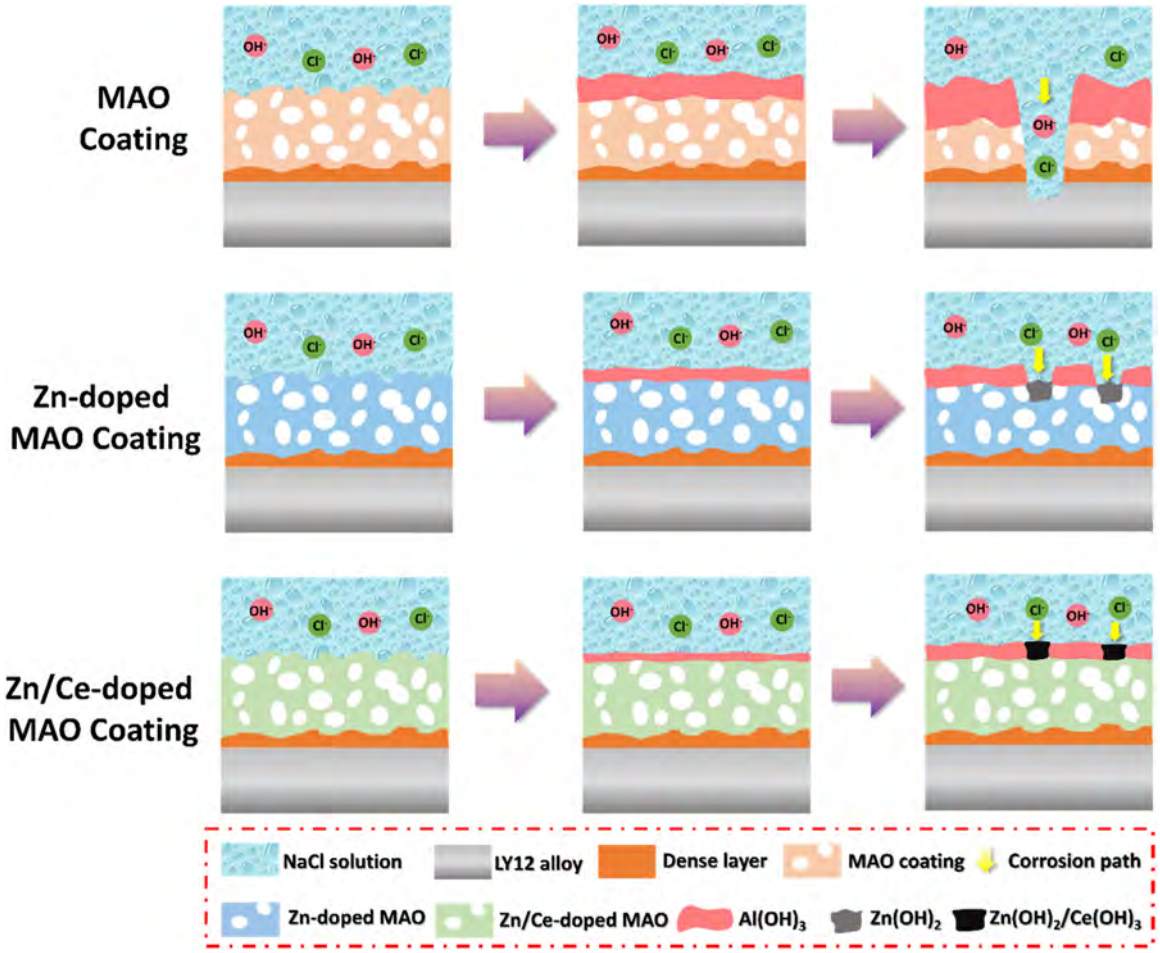

Fig. 8. Schematic illustration of corrosion mechanism of undoped and doped MAO coatings on Al alloy LY12.

tential and resistance. However, during the long-term corrosion process, the zinc phosphate on the surface with a specific K_{sp} will also dissolve, releasing Zn^{2+} that will preferentially react with excess OH^- in the corrosive medium to form the corrosion product $Zn(OH)_2$ at the corrosion interface, as shown by formula (8):

$$Zn^{2+} + 2OH^- \rightarrow Zn(OH)_2 \quad (8)$$

$Zn(OH)_2$ is deposited in the micro-regions to act as a protective barrier, rather than forming the lower K_{sp} zinc phosphate. At the pitting locations, more corrosive medium accumulates, more Zn^{2+} dissolves, and the protective corrosion product of $Zn(OH)_2$ is formed to block the permeation of the corrosive medium.

In MAO coatings doped with zinc phosphate/cerium phosphate, both zinc phosphate and cerium phosphate are distributed throughout the coating in a nanocrystalline structure enveloped by an amorphous substrate. Zinc phosphate tends to generate and accumulate at discharge pitting locations due to the smaller K_{sp}, while cerium phosphate is uniformly dispersed in the coating. During corrosion, $Al(OH)_3$ corrodes the weak pitting areas and is further dissolved by Cl^- to create a corrosion micro-region. In this area, the enriched zinc phosphate dissolves under the influence of Cl^- to produce Zn^{2+}, which rapidly forms the corrosion product of $Zn(OH)_2$. Moreover, cerium phosphate in the coating dissolves Ce^{3+} under the action of Cl^- to form the corrosion product of $Ce(OH)_3$ with a lower K_{sp} at a faster rate, as shown by formula (9):

$$Ce^{3+} + 3OH^- \rightarrow Ce(OH)_3 \quad (9)$$

The corrosion product of $Zn(OH)_2/Ce(OH)_3$ fills the areas where $Al(OH)_3$ has been lost in the corrosion micro-regions with a larger volume, thus ensuring that the coating maintains its integrity even after corrosion. The mixed corrosion product serves the self-filling function to enhance the corrosion resistance.

4. Conclusions

Phosphate is used as main ingredient in MAO electrolyte, while soluble zinc acetate and cerium acetate are chosen as precursors for the formation of zinc phosphate and cerium phosphate. In the MAO process, zinc phosphate and cerium phosphate are produced in situ by micro-arc discharge and enveloped in nanocrystals within an amorphous structure. Zinc phosphate is formed preferentially and concentrated at the discharge pore locations due to its lower K_{sp}. Compared to undoped MAO coating, corrosion potential increases from −1.253 V to −0.819 V_{SCE}, and the corrosion current density decreases by nearly 2 orders of magnitude, from 9.8×10^{-9} to 2.5×10^{-10} A·cm^{-2}. MAO coating doped with zinc phosphate/cerium phosphate shows significantly improved corrosion resistance. During long-term corrosion, zinc phosphate on surface and weak pores in the coating dissolve and release Zn^{2+} under action of Cl^-, forming corrosion products of $Zn(OH)_2$, which covers corrosion micro-regions. Simultaneously, cerium phosphate releases Ce^{3+}, which is deposited as $Ce(OH)_3$ due to smaller K_{sp}, forming $Zn(OH)_2/Ce(OH)_3$ that fills and covers corrosion micro-regions, thereby blocking penetration of corrosive medium to substrate. Co-doped MAO coating significantly improves corrosion resistance of Al alloy LY12 and has large application prospects.

Declaration of competing interest

The authors declare that they have no known competing financial interests or personal relationships that could have appeared to influence the work reported in this paper.

CRediT authorship contribution statement

Chao Yang: Writing – original draft, Project administration, Investigation, Funding acquisition, Data curation, Conceptualization. **Tao Ying:** Visualization, Resources, Formal analysis, Data curation. **Aihui Huang:** Writing – review & editing, Resources, Investigation, Conceptualization. **Jian Huang:** Validation, Software, Methodology, Formal analysis. **Pinghu Chen:** Writing – review & editing, Investigation, Formal analysis, Conceptualization. **Paul K. Chu:** Writing – review & editing, Project administration, Investigation. **Xiaoqin Zeng:** Writing – review & editing, Investigation, Funding acquisition, Conceptualization.

Acknowledgments

This work was financially supported by the National Natural Science Foundation of China (52401101 and 52425101), Postdoctoral Fellowship Program of CPSF (GZC20231545), China Postdoctoral Science Foundation (2024T170557 and 2023M742224), Shanghai Post-doctoral Excellence Program (2023440), and City University of Hong Kong Donation Research Grants (9220061 and DON-RMG 9229021).

References

[1] R.X. Li, B.X. Bian, G. Wilde, Y. Zhang, S.V. Divinski, Grain boundary diffusion in high-Zn-content Al alloys: evidence of grain boundary phase transition induced by Zn segregation, Acta Mater. 277 (2024) 120205.
[2] Z.Y. Zhao, D.X. Li, X.R. Yan, Y. Chen, Z. Jia, D.Q. Zhang, M.X. Han, X. Wang, G.L. Liu, X.F. Liu, S.D. Liu, Insights into the dual effects of Ti on the grain refinement and mechanical properties of hypoeutectic Al-Si alloys, J. Mater. Sci. Technol. 189 (2024) 44–59.
[3] Q. Sun, M. Yang, Y. Jiang, L. Lei, Y. Zhang, Achieving excellent corrosion resistance properties of 7075 Al alloy via ultrasonic surface rolling treatment, J. Alloy. Compd. 911 (2022) 165009.
[4] Y. Lv, T. Hashimoto, X.R. Zhou, X.X. Zhang, Influence of thermomechanical treatment on the corrosion behaviour of 2A97 Al-Cu-Li alloy, Corros. Commun. 15 (2024) 13–23.
[5] Z.Y. Wang, T. Ma, W. Han, G.C. Yu, Corrosion behavior on aluminum alloy LY12 in simulated atmospheric corrosion process, Trans. Nonferrous Met. Soc. China l7 (2007) 326–334.
[6] C. Yang, L.Y. Sheng, C.C. Zhao, D. Wu, Y.F. Zheng, Regulating the ablation of nanoparticle-doped MAO coating on Mg alloy by MgF_2 passivation layer construction, Mater. Lett. 355 (2024) 135559.
[7] R.D. Olmo, M. Mohedano, E. Matykina, R. Arrabal, Permanganate loaded Ca-Al-LDH coating for active corrosion protection of 2024-T3 alloy, Corros. Sci. 198 (2022) 110144.
[8] M.M. Cui, D.I. Njoku, B.W. Li, L.H. Yang, Z.K. Wang, B.R. Hou, Y. Li, Corrosion protection of Aluminium Alloy 2024 through an epoxy coating embedded with smart microcapsules: the responses of smart microcapsules to corrosive entities, Corros. Commun. 1 (2021) 1–9.
[9] F. Muhaffel, M. Baydogan, H. Cimenoglu, A study to enhance the mechanical durability of the MAO coating fabricated on the 7075 Al alloy for wear-related high temperature applications, Surf. Coat. Technol. 409 (2021) 126843.
[10] C. Yang, C.Y. Wang, Z. Shen, L.P. Zhou, L.Y. Sheng, D.K. Xu, Y.F. Zheng, P.K. Chu, S. Xiao, T. Ying, X.Q. Zeng, Simultaneous improvement of wear and corrosion resistance of microarc oxidation composite coatings on ZK61 Mg alloy by doping with ZrO_2 nanoparticles, J. Mater. Sci. Technol. 224 (2025) 312–327.
[11] X.X. Zhang, Y.P. Zhang, Y. Lv, Z.H. Dong, T.R. Hashimoto, X.R. Zhou, Enhanced corrosion resistance of AZ31 Mg alloy by one-step formation of PEO/Mg-Al LDH composite coating, Corros. Commun. 6 (2022) 67–83.
[12] Y. Tang, C.P. Yang, Q.Q. Sun, L.K. Wu, F.H. Cao, Effects of TiC particles on tribological and corrosion resistance of PEO coating on TC4 alloy, Corros. Commun. 14 (2024) 1–10.
[13] C.Y. Li, X.L. Fan, R.C. Zeng, L.Y. Cui, S.Q. Li, F. Zhang, Q.K. He, M.B. Kannan, H.W. Jiang, D.C. Chen, S.K. Guan, Corrosion resistance of in-situ growth of nanosized Mg(OH)2 on micro-arc oxidized magnesium alloy AZ31—Influence of EDTA, J. Mater. Sci. Technol. 35 (2019) 1088–1098.
[14] X. Lu, C. Blawert, K.U. Kainer, M.L. Zheludkevich, Investigation of the formation mechanisms of plasma electrolytic oxidation coatings on Mg alloy AM50 using particles, Electrochim. Acta 196 (2016) 680–691.
[15] A. Alabbasi, A. Mehjabeen, M.B. Kannan, Q.S. Ye, C. Blawert, Biodegradable polymer for sealing porous PEO layer on pure magnesium: an in vitro degradation study, Appl. Surf. Sci. 301 (2014) 463–467.
[16] X. Lu, M. Mohedano, C. Blawert, E. Matykina, R. Arrabal, K.U. Kainer, M.L. Zheludkevich, Plasma electrolytic oxidation coatings with particle additions – A review, Surf. Coat. Technol. 307 (2016) 1165–1182.
[17] J. Liang, P.B. Srinivasan, C. Blawert, W. Dietzel, Comparison of electrochemical corrosion behaviour of MgO and ZrO_2 coatings on AM50 magnesium alloy formed by plasma electrolytic oxidation, Corros. Sci. 51 (2009) 2483–2492.
[18] C. Yang, J. Huang, S.H. Cui, R.K.Y. Fu, L.Y. Sheng, D.K. Xu, X.B. Tian, Y.F. Zheng, P.K. Chu, Z.Z. Wu, NaF assisted preparation and the improved corrosion resistance of high content ZnO doped plasma electrolytic oxidation coating on AZ31B alloy, J. Magnes. Alloy. 12 (2024) 3602–3615.
[19] C. Yang, Z.M. Sun, C.Y. Wang, A.H. Huang, T. Ying, L.P. Zhou, Z.S. Ye, S. Xiao, P.K. Chu, X.Q. Zeng, A self-sealing and self-healing MAO corrosion-resistant coating on aluminum alloy by in situ growth of $CePO_4/Al_2O_3$, Corros. Sci. 245 (2025) 112706.
[20] S.P. Ji, Y.C. Weng, Z.Z. Wu, Z.Y. Ma, X.B. Tian, R.K.Y. Fu, H. Lin, G.S. Wu, P.K. Chu, F. Pan, Excellent corrosion resistance of P and Fe modified micro-arc oxidation coating on Al alloy, J. Alloy. Compd. 710 (2017) 452–459.
[21] E.H. Yang, R.X. Yang, W. Wei, Q.F. Mo, F.Y. Liang, D. Li, W.Z. Li, Corrosion resistance and antibacterial properties of hydrophobic modiffed Ce-doped micro-arc oxidation coating, J. Mater. Res. Technol. 29 (2024) 3303–3316.
[22] Q. Huang, L.L. Liu, Z.Z. Wu, S.P. Ji, H. Wu, P.H. Chen, Z.Y. Ma, Z.C. Wu, R.K.Y. Fu, H. Lin, X.B. Tian, F. Pan, P.K. Chu, Corrosion-resistant plasma electrolytic oxidation coating modified by Zinc phosphate and self-healing mechanism in the salt-spray environment, Surf. Coat. Technol. 384 (2020) 125321.
[23] H.Y. Wang, J. Wang, Y. Yang, T. Ying, Z.F. Xin, N. Hao, W. Huang, X.Q. Zeng, Development of highly corrosion-resistant Mg-Al-Y extruded alloy via regulating the Mg17Al12 phase, Corros. Sci. 234 (2024) 112124.
[24] C.C. Zhao, W.T. Ouyang, M. Wen, C. Yang, D.K. Xu, Y.F. Zheng, T.F. Xi, L.Y. Sheng, Optimizing corrosion resistance of the Mg-4Zn-0.5Y-0.5Nd alloys by regulation of secondary phase and grain structure, J. Mater. Res. Technol. 35 (2025) 435–450.
[25] Q.C. Zhu, Y.X. Li, F.Y. Cao, D. Qiu, Y. Yang, J.Y. Wang, H. Zhang, T. Ying, W.J. Ding, X.Q. Zeng, Towards development of a high-strength stainless Mg alloy with Al-assisted growth of passive film, Nat. Commun. 13 (2022) 5838.
[26] Y.H. Zhang, L.M. Wu, P.P. Huang, Q. Shen, Z.X. Sun, Determination and application of the solubility product of metal xanthate in mineral flotation and heavy metal removal in wastewater treatment, Miner. Eng. 127 (2018) 67–73.
[27] C. Yang, C.Y. Wang, X.Z. Zhao, Z. Shen, M. Wen, C.C. Zhao, L.Y. Sheng, Y.G. Wang, D.K. Xu, Y.F. Zheng, P.l K. Chu, X.Q. Zeng, Superhydrophobic surface on MAO-processed AZ31B alloy with zinc phosphate nanoflower arrays for excellent corrosion resistance in salt and acidic environments, Mater. Des. 239 (2024) 112769.
[28] M.J. Dai, Y.F. Cheng, Z. Wang, F. Huang, Q. Hua, J. Liu, Understanding pit initiation of pipeline steel X100 under cathodic protection potential fluctuating with various duty cycles, Corros. Commun. 12 (2023) 11–18.
[29] J. S´wiatowska, V. Lair, C. Pereira-Nabais, G. Cote, P. Marcus, A. Chagnes, XPS, XRD and SEM characterization of a thin ceria layer deposited onto graphite electrode for application in lithium-ion batteries, Appl. Surf. Sci. 257 (2011) 9110–9119.
[30] N.V. Phuong, M. Gupta, S. Moon, Enhanced corrosion performance of magnesium phosphate conversion coating on AZ31 magnesium alloy, Trans. Nonferrous Met. Soc. China 27 (2017) 1087–1095.
[31] J. Jayaraj, S. Arun Kumar, A. Srinivasan, K.G. Raghu, C. Arunchandran, V. Rajinikanth, Corrosion and in vitro characteristics of cerium phosphate based chemical conversion coating on AZ31 magnesium alloy, Appl. Surf. Sci. 644 (2024) 158797.
[32] J. Qin, X.T. Shi, H.Y. Li, R.F. Zhao, G.Q. Li, S.F. Zhang, L.Y. Ding, X.J. Cui, Zhao Y, R.F. Zhang, Performance and failure process of green recycling solutions for preparing high degradation resistance coating on biomedical magnesium alloys, Green. Chem. 24 (2022) 8113.
[33] Y.C. Zou, Y.M. Wang, S.M. Xu, T. Jin, D.Q. Wei, J.H. Ouyang, D.C. Jia, Y. Zhou, Superhydrophobic double-layer coating for efficient heat dissipation and corrosion protection, Chem. Eng. J. 362 (2019) 638–649.
[34] A. Jangde, S. Kumar, C. Blawert, Influence of glycerol on plasma electrolytic oxidation coatings evolution and on corrosion behaviour of coated AM50 magnesium alloy, Corros. Sci. 157 (2019) 220–246.
[35] J.Q. Feng, Y.B. Wang, F.X. Tao, Y.K. Li, K.Z. He, Z.B. Xu, H.Q. Tang, Z.D. Wang, Effect of tensile cracks on the corrosion protection properties of anodic oxide films on 5083 Al alloy, J. Alloy. Compd. 997 (2024) 174950.
[36] P. Deng, W.F. Mo, Z.Q. Ouyang, K. Ling, B.H. Luo, Z.H. Bai, Microstructural evolution and corrosion mechanism of micro-alloyed 2024 (Zr, Sc, Ag) aluminum alloys, Corros. Sci. 224 (2023) 111476.
[37] C.Y. Wang, M.S. Sun, C. Yang, H.Y. Wang, J. Wang, L. Mao, Y. Yang, T. Ying, P.K. Chu, X.Q. Zeng, Degradation behavior of pure Mg in the physiological medium and growth mechanism of surface corrosion product films, J. Magnes. Alloy. https://doi.org/10.1016/j.jma.2024.05.012.
[38] B. Zaid, D. Saidi, A. Benzaid, S. Hadji, Effects of pH and chloride concentration on pitting corrosion of AA6061 aluminum alloy, Corros. Sci. 50 (2008) 1841–1847.